

# Drop-shaped microgrooves guide unidirectional cell migration for enhanced endothelialization

Received: 14 November 2024

Accepted: 11 February 2025

Published online: 24 February 2025

Xing-wang Wang<sup>1</sup>, Cheng-qiang Ye<sup>1</sup>, Qian Tang<sup>2,3</sup>, Hong-mei Yu<sup>4</sup>, Jing Wang<sup>1,5</sup>, Guo-sheng Fu<sup>2,3</sup>, Ke-feng Ren<sup>1,2,3</sup>✉, Lu Yu<sup>2,3</sup>✉ & Jian Ji<sup>1,5</sup>✉

Atrial fibrillation (AF) significantly increases the risk of ischemic stroke, and in non-valvular AF, 90% of stroke-causing thrombi arise from the left atrial appendage (LAA). Percutaneous LAA occlusion using an occluder is a crucial clinical intervention. However, occluder materials could provoke thrombi, termed device-related thrombosis (DRT), leading to treatment failure. Rapid endothelialization is essential to address the DRT but the occluder's large surface area and irregular cell migration on the surface impede this process. Here, we report a continuous drop-shaped microgroove, which has a drop-shaped unit structure similar to endothelial cells. The microgrooves polarize the cytoskeleton, guiding cell unidirectional migration within the grooves, and increase cell migration efficiency. We show that drop-shaped microgrooves accelerate wound healing in a rat model, and that occluder discs with drop-shaped microgrooves promote endothelialization in a canine model. Together, our results show that integrating microgrooves with medical devices is a promising approach for addressing DRT.

Atrial fibrillation (AF), a prevalent arrhythmia, impacts 2–4% of adults globally. AF is associated with a 5-fold increased risk of ischemic stroke and systemic embolism<sup>1</sup> and is responsible for 25% of ischemic strokes in aged patients<sup>2,3</sup>. Acute ischemic stroke patients with AF have higher mortality, poorer functional outcomes, greater risk of intracerebral hemorrhage<sup>2</sup>. Percutaneous closure of left atrial appendage (LAA) with occluders is an increasingly adopted strategy to reduce stroke risk in patients with AF, significantly lowering the rates of stroke and systemic embolism<sup>4,5</sup>.

Commercial LAA occluders are typically composed of a nitinol metal framework and a polyethylene terephthalate (PET) fiber membrane<sup>6</sup>. The occluder disk diameter is approximately 2–4 centimeters. Due to the relatively poor biocompatibility of the constituent

materials and the large surface area of the occluder disk<sup>7</sup>, endothelialization of the disk surface typically requires 1 to 3 months<sup>8</sup>. Some patients have not yet endothelialized even 2 to 3 years after the occluder is implanted<sup>9,10</sup>. Before complete endothelialization, there is a potential risk of causing device-related thrombosis (DRT)<sup>11,12</sup>. The thrombosis will cause more severe systemic embolism. Therefore, accelerating the coverage of neo-tissue on the surface of the occluder and promoting endothelialization becomes important strategies to address DRT<sup>13–15</sup>. Guiding cells to migrate in a certain direction on the surface of an occluder disk may significantly accelerate the speed of endothelialization<sup>16</sup>. Research has shown that surface topography is an effective means of guiding migration<sup>17,18</sup> and accelerating the healing process<sup>19,20</sup>. Parallel microgrooves can restrict the direction of cell

<sup>1</sup>MOE Key Laboratory of Macromolecular Synthesis and Functionalization, Department of Polymer Science and Engineering, Zhejiang University, Hangzhou, China. <sup>2</sup>Key Laboratory of Cardiovascular Intervention and Regenerative Medicine of Zhejiang Province, Department of Cardiology, Sir Run Run Shaw Hospital, Zhejiang University, Hangzhou, China. <sup>3</sup>Engineering Research Center for Cardiovascular Innovative Devices of Zhejiang Province, Hangzhou, China. <sup>4</sup>Department of Surgery, Sir Run Run Shaw Hospital, Zhejiang University, Hangzhou, China. <sup>5</sup>State Key Laboratory of Transvascular Implantation Devices, The Second Affiliated Hospital Zhejiang University School of Medicine, Hangzhou, China. ✉e-mail: [renkf@zju.edu.cn](mailto:renkf@zju.edu.cn); [jiyu@zju.edu.cn](mailto:jiyu@zju.edu.cn); [jijian@zju.edu.cn](mailto:jijian@zju.edu.cn)

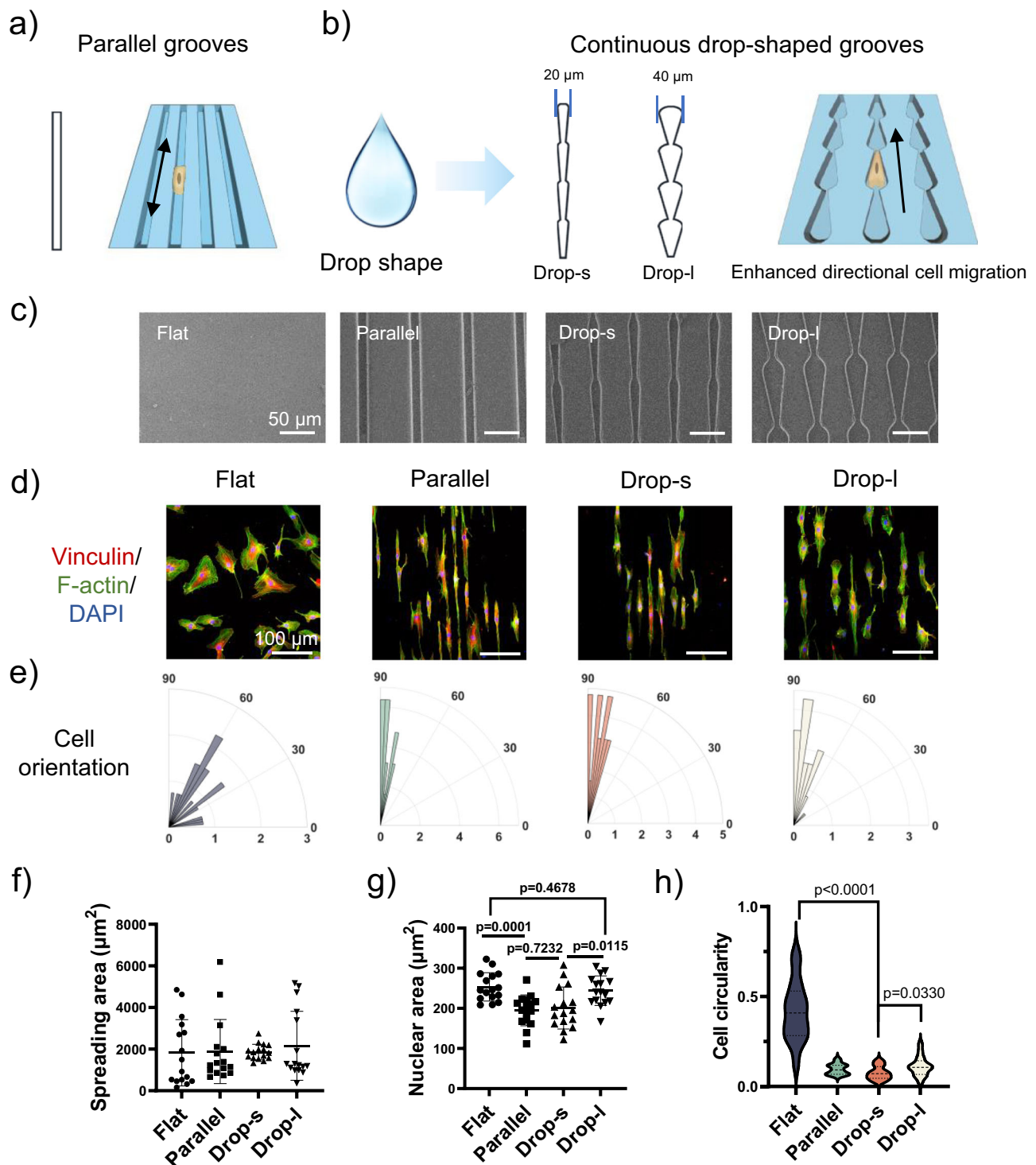


**Fig. 1 | The interactions between different microgrooves and cells. a** Schematic diagram of parallel microgrooves and their influence on cell migration. **b** Schematic diagram of drop-shaped microgrooves and their influence on cell migration. **c** Scanning electron microscope (SEM) images of the flat surface, parallel microgrooves, and drop-shaped grooves. Scale bars, 50  $\mu\text{m}$ . **d** Confocal microscopy images of cells spreading on different surfaces. Scale bar, 100  $\mu\text{m}$ . Statistics of cells

orientation degree (**e**), cell spreading area (**f**) ( $n=16$  cells from three technical replicates), nuclear area (**g**) ( $n=16$  cells from three technical replicates), and cell circularity (**h**) ( $n=16$  cells from three technical replicates) on different surfaces. Data are presented as means  $\pm$  standard deviation (SD). Significance determined by unpaired two-tailed  $t$ -test (**f–h**).

migration, promote the migration<sup>21,22</sup> and maturation of endothelial cells<sup>23</sup>, and thereby accelerate endothelialization<sup>24–26</sup>. Some findings also suggest that introducing asymmetric structures into cell migration paths can further restrict the direction of cell migration, such as ratchet-shaped grooves<sup>27–29</sup>.

Therefore, in this study, we hypothesize that guiding the directional migration of cells on the surface through local microtopography can accelerate endothelialization. Inspired by the ratchet-shaped grooves, here we design microgrooves composed of a continuous series of drop shapes. We observe that cells tend to migrate from the

wider part of the drop towards the narrower part, crossing the 'neck' to enter the wider section, and repeating this process. Reverse migration of cells is limited. In this microgroove, there is only one direction for cell migration. By arranging these drop-shaped microgrooves on specific surfaces, we find that this configuration can enhance the collective migration efficiency of cells, accelerating the coverage of the surface by cells and tissue. We further apply this kind of microgroove to the surface of occluder discs, confirming its ability to expedite endothelialization. Our research presents a surface microstructure design that effectively accelerates endothelialization on the surfaces of interventional medical devices.

## Results

### Microgrooves alter cell morphology

We first demonstrated the design of drop-shaped microgrooves (Fig. 1a, b, Supplementary Fig. 1). Compared to ordinary parallel microgrooves (Fig. 1a), we designed two sizes of drop-shaped microgrooves (Drop-s and Drop-l) (Fig. 1b). The characteristic of drop-shaped microgrooves is that they have local asymmetry on the cell migration path. We anticipate that this asymmetry could restrict the direction of cell migration. In ordinary parallel microgrooves, there are two directions for cell migration<sup>21</sup>, while in grooves with local asymmetry, the direction of cell migration is usually limited to a single direction (Fig. 1a, b). To compare whether different types of microgrooves have the same ability to restrict cell morphology, we first studied the cell morphology on flat surfaces and grooves with different patterns (Fig. 1d–h). On flat surfaces, cells had fully spread out and were approximately circular. On various grooved surfaces, the spreading of cells was restricted, and cells were elongated along the direction of the grooves, resembling a bar shape. Cells on grooved surfaces showed an obvious orientation along the groove direction. The parallel grooves and drop-shaped microgrooves had a similar restricting effect on cells; on larger drop-shaped microgrooves (Drop-l), the cells spread out over a larger area, and their shapes deviated slightly from the bar shape. The restriction imposed by the microgrooves was also transmitted to the cell nuclei. The area of cell nuclei on grooved surfaces was significantly reduced. We also examined the adhesion and proliferation of cells on flat and different microgroove surfaces (Supplementary Fig. 2a). Microgrooves do not have a significant impact on cell adhesion and proliferation (Supplementary Fig. 2b). These results indicate that continuous drop-shaped microgrooves and parallel microgrooves can both restrict the cytoskeleton, and the restricting ability is related to the average width of the grooves. Local variations in width have no significant effect on cell shape and size.

### The drop-shaped microtopography directs unidirectional cell migration

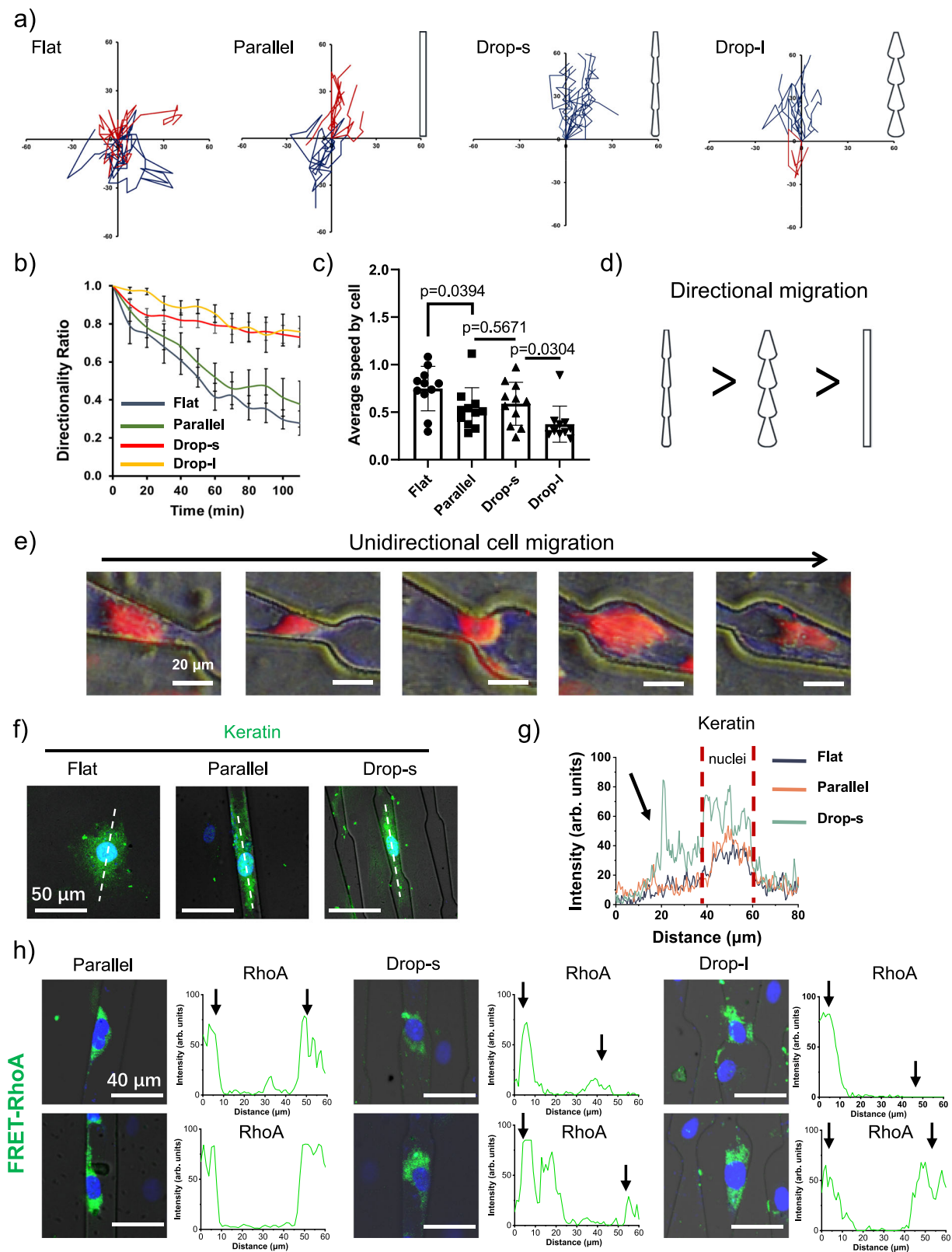
We further investigated the state of cell migration on flat surfaces and surfaces with different groove structures. As shown in Fig. 2a, cells migrate in random directions on flat surfaces. On parallel microgrooves, cells exhibit clear migration in two directions along the grooves. However, on drop-shaped microgrooves, the direction of cell migration is significantly restricted. Cells almost exclusively migrate from the wider end to the narrower end of the droplet. This restrictive effect is more pronounced in the narrower droplets. We further quantified the directionality of cell migration. The results show that cells on drop-shaped microgroove surfaces exhibit higher directional correlation, indicating that the asymmetry on the migration path successfully limits the direction of cell migration, with cells continuously moving from the tail to the tip of the droplet. We statistically analyzed the migration speed of cells on different surfaces. The migration speed of cells is related to the width of the grooves. Cells move slower on groove surfaces, and their migration speed is even slower on wider grooves. Grooves can provide guidance cues for cell

migration. However, wider grooves may cause the cell to have more difficulty in orienting itself properly for migration. Cells tend to align with the grooves and migrate along them. But if the grooves are too wide, the cell may receive conflicting or less precise guidance signals. This misorientation can lead to inefficient movement patterns, such as zig-zagging or stalling, which ultimately results in a slower migration speed<sup>21</sup>.

To study the effect of local asymmetry on the directional migration of cells, we further observed the movement state of cells in different areas through live cell staining and immunofluorescence labeling. Figure 2e demonstrates the migration process of cells within drop-shaped microgrooves. Cells migrated from the tail to the tip of the droplet, contracting as they passed through the neck, then spreading out at the tail of the droplet, repeating this cycle. The changes in the cytoskeleton were closely related to the distribution of actin and keratin. We labeled keratin to study the changes in keratin density during migration on different surfaces (Fig. 2f). Within the drop-shaped microgrooves, a clear polarization of keratin distribution was observed as cells passed through the neck. Keratin accumulated at the trailing edge of migration. This indicates that due to the presence of the asymmetric structure, when cells move from the wider area of the droplet over the neck into the narrower area, keratin spontaneously assembles at the trailing edge, propelling cell migration. Rho signaling can also control migration through its effects on the microtubule network organization and stability. Rho promotes the formation of longer-lived or highly stable structures such as stress fibers and stable microtubules that are oriented in the direction of migration. As shown in Fig. 2h, the signal intensity of RhoA within cells also exhibited a polarized distribution on the surface of the drop-shaped microgrooves. These results indicate that cells migrating on drop-shaped microgrooves tend to move from the wider to the narrower end of the droplets, while migration in the reverse direction is significantly inhibited.

### The drop-shaped microgrooves enhance the collective migration of cells

We further designed experiments to investigate whether the migration patterns of single cells on locally asymmetric grooves would affect collective cell migration. First, we simulated cell migration on different surfaces with MATLAB (Fig. 3a–d). Within a square area, there are cells that need to cover the central red circle. We incorporated the directionality and migration speed of single cells into the code to determine the process of cells covering the circle. As shown, cells cover the circle significantly faster on the surface of drop-shaped grooves, with velocity streamlines converging towards the center. This effect is more pronounced with narrower drop-shaped microgrooves (Drop-s), where cell coverage is even faster. The direction of cell velocity vectors also confirms that on the surface of drop-shaped grooves, cell migration direction is more concentrated (towards the center). We validated this simulation with cell experiments. We created a 2 mm diameter circular area devoid of cells, with cells migrating from outside the area to cover the central region (Fig. 3e). We selected the immortalized human microvascular endothelial cells (HMEC/D3) with faster migration speeds for our experiments. We quantified the progress of cell coverage of the central area at different time points (Fig. 3f, Supplementary Fig. 4). Compared to flat surfaces and parallel microgrooves, the speed of cell coverage of the central area on the drop-shaped groove surfaces was significantly faster, with the Drop-s surface being the fastest, which is consistent with the results of single-cell migration. During collective migration, cell migration against the groove direction on the Drop-s and Drop-l was effectively inhibited (Supplementary Fig. 5). We also verified the coverage speed of human umbilical vein endothelial cells (HUVECs), and smooth muscle cells (SMC), which are related to endothelialization, on different surfaces (Fig. 3h). On the Drop-s surface, these cells all exhibited faster



coverage speeds. This suggests that the drop-shaped microgrooves can accelerate the migration of various cells related to endothelialization. But the promoting effect on SMC migration was relatively weak. The length of SMCs is approximately 200–240  $\mu\text{m}$ , which is about three times the length of a single drop unit of drop-shaped microgroove (Supplementary Fig. 3). Therefore, SMCs are less sensitive to the local asymmetry of the microgrooves. We infer that fabricating the

Drop-s structure on the surface of an occluder may be beneficial for the endothelialization of the LAA occluder surface.

### The drop-shaped microgrooves facilitate tissue formation and coverage

Before verifying the role of Drop-s microgrooves in accelerating endothelialization of the LAA occluder, we first investigated the



**Fig. 2 | Migration behavior of HUVECs on the surface with different topographies.** **a** Cell trajectories ( $n = 11$ – $12$  cells) after 2 h of migration on the flat surface or on different microgrooves. Statistical analysis of the **b** directionality ratio and **c** speed of cell migration on different surfaces ( $n = 11$  cells). **d** Comparative analysis of cell migration directionality on different surfaces. **e** Cell migration process in drop-shaped microgrooves. Red: CellTracker™ orange. Scale bars are 20  $\mu\text{m}$ . **f** Staining of keratin (green) and nuclei (blue) of HUVECs migrated on different surfaces. **g** Quantitative analysis of keratin intensity on different surfaces. The red

line indicates the nuclei area. The black arrow represented the RhoA polarization signal. **h** Staining of RhoA (green) and nuclei (blue) of HUVECs migrated on different surfaces and the quantitative analysis of RhoA fluorescence intensity changes. RhoA activity was detected using fluorescence resonance energy transfer (FRET) biosensor. The black arrow represented the RhoA polarization signal. The data were representative of three independent experiments and expressed as the mean  $\pm$  standard deviation (SD). Data are presented as means  $\pm$  SD. Significance determined by unpaired two-tailed  $t$ -test (**c**).

interaction between Drop-s microgrooves and tissue. We designed a rat back wound healing experiment to investigate whether Drop-s could promote the migration of surrounding cells to accelerate tissue healing (Fig. 4a). We placed surfaces with flat and various structured patterns under the wounds, in close contact with them, and observed the wound healing situation after 14 days. Wounds in contact with Drop-s microgrooves healed significantly faster than those in contact with flat surfaces (Fig. 4b, c). We further compared the tissue healing of different surfaces through histological sections (Fig. 4d–f). The results of Hematoxylin and Eosin (H&E)-stained sections of the wound cross-sections showed that the wounds on the Drop-s surfaces were shorter, and there were fewer inflammatory cells in the newly formed tissue. Quantitative statistics revealed that the Drop-s surfaces exhibited greater collagen deposition and fewer inflammatory cells. We investigated angiogenesis through immunofluorescence staining. Vessel formation in the newly formed tissue was correlated with the migration of endothelial and smooth muscle cells. In the newly formed tissue in contact with flat surfaces and parallel microgrooves, there was a larger vascular area with fewer blood vessels, while in the tissue in contact with the Drop-s surfaces, there was a higher vascular density with smaller vascular areas (Fig. 4g–i). This phenomenon indicates that endothelial cells on the Drop-s surfaces migrated more rapidly, favoring the formation of smaller and more numerous blood vessels<sup>30,31</sup>. Further immunofluorescent labeling of immune cells revealed that the density of CD206-positive cells was higher in the newly formed tissue on the Drop-s surfaces (Fig. 4j, k). These results indicate that tissue healing progresses more rapidly on Drop-s surfaces. Subsequent quantitative polymerase chain reaction (qPCR) analysis also confirmed that genes related to wound healing and angiogenesis were highly expressed in the newly formed tissue on Drop-s surfaces (Fig. 4l, m). To verify whether these results were mediated by the surface microstructures, we isolated the newly formed tissue in contact with the samples and performed immunolabeling on the tissue surface (Fig. 4n). We labeled surface collagen (Fig. 4o) and scanned the collagen distribution on the tissue surface using laser confocal microscopy. On the surfaces of parallel microgrooves and drop-shaped microgrooves, collagen exhibited a certain degree of oriented arrangement. Among them, the collagen alignment was more orderly on the Drop-s surfaces (Fig. 4p). This suggests that the microstructures successfully guided the alignment of surface cells, leading to a more regular collagen arrangement, which ultimately affected the entire newly formed tissue and accelerated the tissue healing process.

### The drop-shaped microgrooves accelerate endothelialization on the surface of LAA occluder

Although we have demonstrated that drop-shaped microgrooves successfully accelerated cell migration in vitro and could guide tissue coverage on their surfaces, we still needed to verify whether such microgrooves could practically enhance endothelialization in vivo. We combined surfaces with flat or drop-shaped microgrooves onto the occlusion membrane of an LAA occluder and implanted it into the LAA of canines (Fig. 5a). The occluders were retrieved at 7 days and 14 days post-implantation to assess the degree of endothelialization on the surfaces (Fig. 5b). The occluders were implanted under the guidance of

digital subtraction angiography (DSA) and the post-implant angiography was performed to confirm the appropriate closure of LAA (Fig. 5c). Before the occluder was explanted, its position and residual shunting were also assessed to confirm that the occluder was in a normal state. We conducted gross examinations on the occluders retrieved at different time points (Fig. 5d, e). On day 7, the occlusion membrane covered with flat polydimethylsiloxane (PDMS) had less neo-tissue coverage, with visible exposed metal wire rods. In contrast, the occlusion membrane covered with Drop-s microgrooved PDMS had a thicker layer of neo-tissue with no apparent exposed metal wire rods. The results at day 14 were similar, with the flat PDMS-covered occlusion membrane showing slow progress in neo-tissue coverage and still having exposed metal wire rods. In contrast, the Drop-s microgrooved PDMS-covered occlusion membrane was covered with a thicker layer of tissue.

To investigate the role of microgrooves in accelerating tissue coverage on the surface, we conducted histological analysis of the neo-tissue on the occlusion membrane. At day 7, the neo-granulation tissue density on the Drop-s occlusion membrane was higher, with some blood cells present in the tissue and collagen already densely accumulated (Fig. 6a). A clear vWF signal was observed at the edge of the neo-granulation tissue on the Drop-s occlusion membrane, indicating that endothelialization had begun. However, on the flat occlusion membrane, the collagen in the neo-granulation tissue was loosely arranged, with lower density, and there was no clear vWF signal at the edge (Fig. 6a). We also marked myofibroblasts in the tissue sections with alpha Smooth Muscle Actin ( $\alpha\text{SMA}$ ) (Fig. 6a). Near the occlusion membrane, there were significantly more fibroblasts near the Drop-s surface, indicating that the fibrotic process of the tissue was also progressing more rapidly. By day 14, the differences were more pronounced (Fig. 6b). The neo-tissue on the Drop-s occlusion membrane was almost mature, with neatly arranged collagen and a clear von Willebrand factor (vWF) signal at the tissue edge. In the tissue sections, fibroblasts were densely distributed in an elongated pattern. The section results indicated that the occlusion membrane with Drop-s microgrooves successfully promoted the coverage and endothelialization of the surface neo-tissue. Further quantitative results highlighted the differences in tissue regeneration progress on different surfaces at 7 and 14 days (Fig. 6c–e). During the initial 7 days, collagen accumulation on the Drop-s surface was faster, and by day 14, the density on the Drop-s and Flat surfaces reached a comparable level. However, endothelialization and fibrotic progression on the Drop-s surface were consistently faster, especially during the first 7 days. This indicates that the drop-shaped microgrooves successfully accelerated early cell coverage. To investigate the correlation between cell migration and these processes, we further marked RhoA (Fig. 6f). Immunofluorescence staining results showed that the area of RhoA-positive regions in the tissue on the Drop-s surface was larger (Fig. 6g), suggesting that cell migration was more active on the Drop-s surface. Based on the histological section results, we quantified the arrangement of collagen and fibroblasts in the neo-tissue on different surfaces (Fig. 6h, i, Supplementary Fig. 6). The results showed that Drop-s microgrooves successfully guided the directional arrangement of the neo-tissue. In summary, the results on the occluder were similar to the in vitro experiments, with the drop-shaped microgrooves successfully

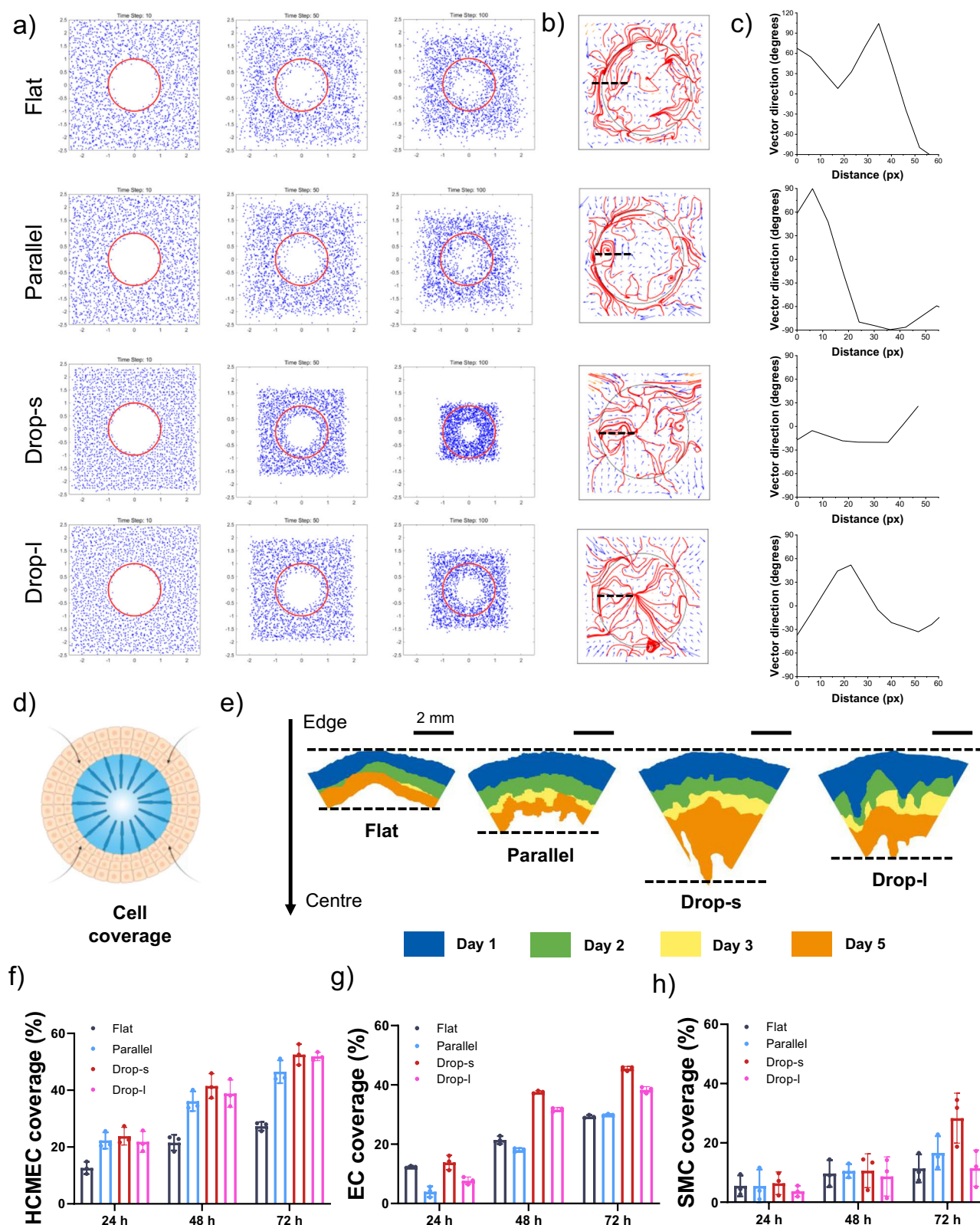
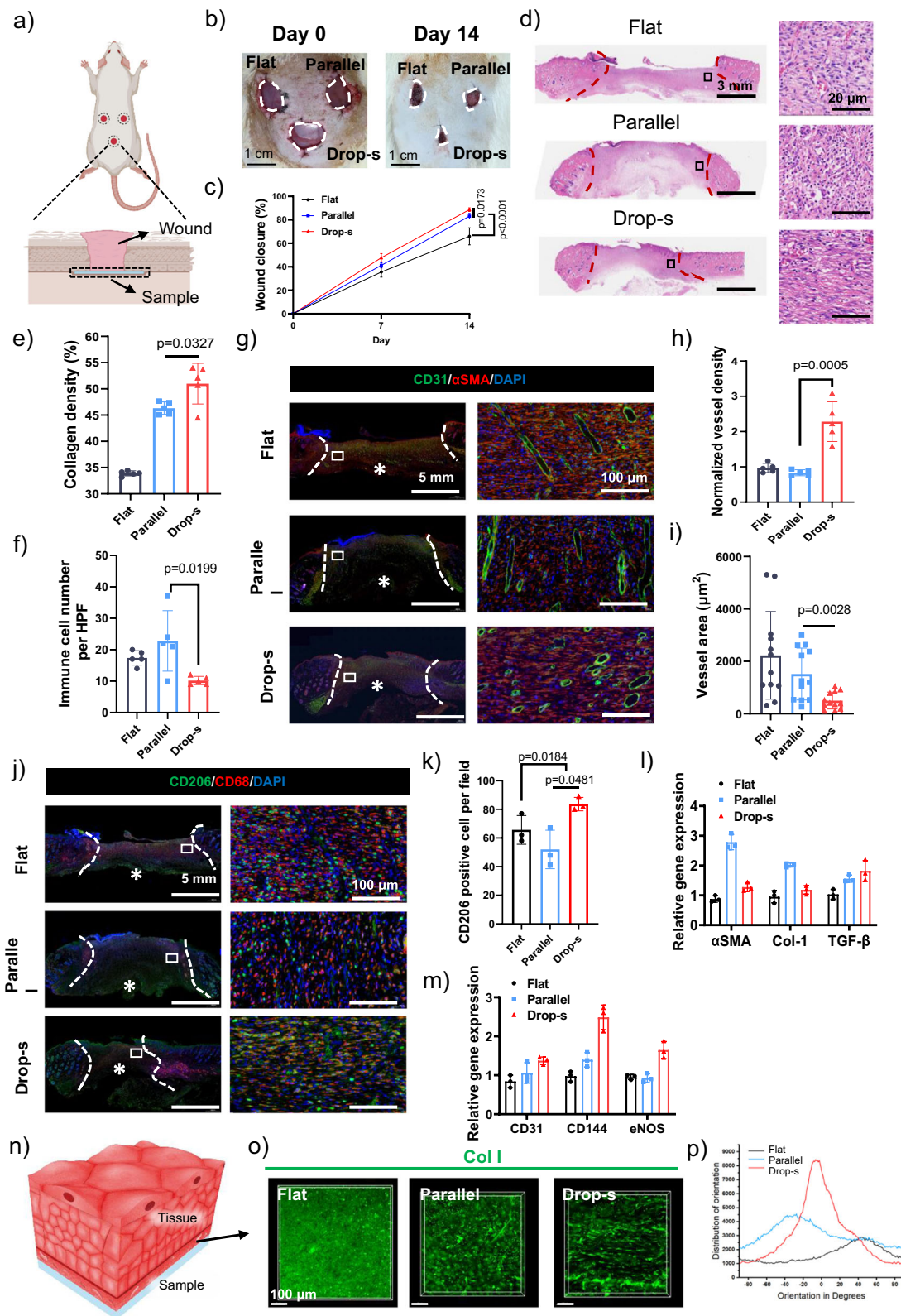


**Fig. 3 | Simulation and characterization of cell collective migration on different surfaces.** **a** Simulation diagram of the degree of cell coverage in the central area changing over time. **b** Cell migration velocity streamline diagram. The black dashed line represents the sampling location for velocity direction. **c** Cell migration velocity direction diagram at dashed line position. **d** Schematic diagram of collective cell migration experiment. Created in BioRender. Ji, J. (2025) <https://BioRender.com/m39n040>.

**e** Diagram of cell migration area towards the central region on different surfaces over time. The black dashed line indicates the farthest position of cell migration. **f** Diagram of the percentage of the central area covered by HCMEC (**f**), HUVEC (**g**), and SMC (**h**) on different surfaces over time ( $n = 3$  technical replicates). Data are presented as means  $\pm$  SD (**f–h**).



guiding the initial cell alignment and migration, accelerating collagen accumulation, and tissue maturation.

#### RNA-seq analysis of endothelialization on the LAA occluder accelerated by drop-shaped microgrooves

To further confirm the impact of flat surfaces and microgrooves on the endothelialization and tissue healing processes on their surfaces, we

performed transcriptome sequencing on the neo-tissue from different surfaces on day 7. First, we presented the overall gene expression differences through the heatmap and volcano plot analysis of differentially expressed genes (Fig. 7a, b). Compared to the tissue samples from the Flat surfaces, there were 1687 upregulated genes and 1623 downregulated genes in the tissue samples from the Drop-s surfaces. We further analyzed the parameters using gene ontology (GO)



**Fig. 4 | Rat wound healing experiment to assess the interaction between microstructures and tissue.** **a** Schematic diagram of the experimental design. Created in BioRender. Ji, J. (2025) <https://BioRender.com/v94a954>. **b** Photos and statistical data (c) of wound area ( $n = 3$  rats per group). **d** Photos of H&E staining on wound cross-sections (left) and the enlarged image (right). Collagen density (e) and immune cell density (f) counts in H&E staining images (Five measurements of collagen density and immune cell density were taken for 5 different fields of view from 3 rats per group). **g** Images of CD31 staining (green),  $\alpha$ SMA staining (red) and DAPI (blue) on wound cross-sections (left) and the enlarged image (right). Vessel density (h) and vessel area (i) counts in the immunofluorescence staining images (Five measurements of vessel density and twelve measurements of vessels area were taken for 5 different fields of view of 3 rats per group). **j** Images of

CD206 staining (green), CD68 staining (red) and DAPI (blue) on wound cross-sections (left) and the enlarged image (right) ( $n = 3$  rats per group). **k** CD206-positive cells density in the immunofluorescence staining images ( $n = 3$  rats per group). Relative expression of genes about tissue regeneration (l) and angiogenesis (m). ( $n = 3$  rats per group). **n** Schematic diagram of the tissue-sample interface. The black dashed line indicates the interface position. Created in BioRender. Ji, J. (2025) <https://BioRender.com/a99k506>. **o** Laser confocal scanning images of collagen staining in tissue contacting different surfaces. Green: Collagen I (Col I). **p** Statistics of collagen fiber orientation in tissue contacting different surfaces. The data were representative of three independent experiments and expressed as the mean  $\pm$  SD. Significance determined by unpaired two-tailed *t*-test (c, e, f, h, i, k) and  $p > 0.05$  was considered as not significant.

classification analysis. The GO enrichment analysis bubble chart revealed that the differentially expressed genes were primarily enriched in genes related to cytoskeletal changes, collagen arrangement and remodeling, and cell migration. We used a gene enrichment circle chart to display the core genes with higher association with collagen fibril organization, cell migration, actin cytoskeleton organization, and wound healing. The core genes mainly include Rho family genes (RhoU) and collagen-related genes (CORO1A). This is consistent with the observations from in vitro cell experiments and histological analysis. We further listed the heat maps of gene expression changes related to collagen organization, actin cytoskeleton organization, cell motility, and tissue regeneration. Genes that are positively correlated with these processes show significant upregulation. This indicates that the Drop-s microgrooves on the surface of the occluder can promote cell migration by regulating the cytoskeleton of surface cells and facilitating the arrangement of surface collagen fibers, ultimately accelerating tissue regeneration on the surface.

## Discussion

Cell migration is essential for fundamental physiological processes such as development, tissue repair, and endothelialization<sup>32,33</sup>. In this study, our goal is to restrict cell migration direction by introducing asymmetric factors on the cell migration path, guide unidirectional cell migration, and thus accelerate the endothelialization of the device surface. We first demonstrated that both drop-shaped and parallel microgrooves could restrict cell morphology by affecting the cytoskeleton. However, the drop-shaped microgrooves with local asymmetry on the cell migration path successfully restricted cell migration to a single direction. When cells migrate forward in the drop-shaped grooves and cross the “neck” (cross from the narrow part of the drop into the wide part), integrins accumulate at the sites where the cells contact the groove walls<sup>34</sup>. The cells sense the uneven physical stress in the “neck” region through integrins. This stress distribution is transmitted to the interior of the cells through the cytoskeleton, guiding the polarized distribution of keratin and focal adhesions<sup>35</sup>. The reorganization of the keratin network can regulate the distribution and arrangement of actin filaments<sup>36</sup>, enabling the actin-myosin contraction to be carried out more effectively at the trailing edge of the cells, thus propelling the cells to move forward and cross the bottleneck. The RhoA pathway is an important pathway for regulating the contractile force of actin-myosin<sup>37</sup>. We also observed significant expression of RhoA at the rear of the cell migration path in both Drop-s and Drop-l microgrooves, further confirming the directionality of cell migration<sup>38</sup>. If the cells attempt to cross the “neck” in the reverse direction (cross from the wide part of the drop into the narrow part), the significant size difference cannot polarize the cells. Therefore, the drop-shaped grooves effectively guide the unidirectional migration of cells.

Cell migration is closely linked to tissue healing and endothelialization processes<sup>39</sup>. Although many studies have confirmed through cell experiments that the microgrooves could promote cell migration, the in vivo effects of microgrooves are not well understood. In this work, we conducted validation regarding the interaction between

microgrooves and tissue. We first assessed the interaction of drop-shaped microgrooves with tissue through a wound healing model. We found that the tissue regeneration guided by the drop-shaped microgrooves on the surface was faster, with more orderly collagen arrangement in the tissue in contact with the microgrooves, denser collagen in the neo-tissue, and less inflammation. This indicates that the microgrooves we designed promote tissue regeneration more effectively than traditional parallel microgrooves. Based on these results, we arranged this microstructure on the occluder membrane surface, assembled it into an occluder, and verified its ability to promote endothelialization in a canine model. At both the 7-day and 14-day time points, the animal experiments showed similar results, with tissue maturity and endothelialization progress on the drop-shaped microgrooved surfaces being significantly faster compared to flat surfaces. We demonstrated that this phenomenon is related to the microgrooves guiding cell alignment and accelerating migration through immunohistochemistry and RNA-seq analysis.

Our study also has certain limitations. First, our in vitro cell migration experiments were carried out in a static environment. Flow is critical in EC migration<sup>40</sup>. However, the flow direction and speed of blood near the left atrial appendage are relatively complex<sup>41</sup>. Some of the blood returning from the pulmonary veins enters the left atrial appendage, and a certain vortex-like blood flow will form inside the left atrial appendage. This is because the shape of the left atrial appendage is irregular, presenting as a long tubular or hooked shape, with many trabeculae and pectinate muscle structures inside, causing the blood to turn and swirl when entering and leaving the left atrial appendage<sup>42</sup>. In this situation, it is difficult to simulate the impact of the real blood flow environment in the left atrial appendage on the migration of endothelial cells in vitro. It has been reported in the literature that unidirectional flow can promote cell migration<sup>43</sup>. Whereas, the turbulent blood flow in the left atrial appendage may offset the influence of the blood flow direction on cell migration. Second, the impact of the microgrooves we designed on early thrombosis and inflammation remains unclear. Early DRT is related to local inflammation and thrombosis<sup>42</sup>. However, the micron-sized grooves in our study have little effect on platelet adhesion and activation (Supplementary Fig. 7), because platelets are relatively small in size (1–3  $\mu$ m)<sup>44</sup>. Currently, it has been mainly reported that submicron-sized micropillars/microgrooves or nanoscale surface roughness can reduce platelet adhesion and activation<sup>45</sup>. Regarding the inflammatory response, there are reports in the literature that microstructures guiding macrophage elongation are conducive to polarization towards the M2 phenotype<sup>46</sup>. We observed less inflammation on the Drop-s surface in the wound healing model. However, on the surface tissue of the LAA occluder, the difference in inflammation is relatively small.

Another aspect that needs to be discussed is the transferability of in vitro studies to the clinical used LAA occluders. There are usually two types of occluders: the ball-type LAA occluder such as Watchman LAA occluder (Boston Scientific, Marlborough, Massachusetts, America), and the disk-type occluder such as the LAmbré LAA occluder (Lifetech Scientific Corp., Shenzhen, China)<sup>6</sup>. We selected the disk-type



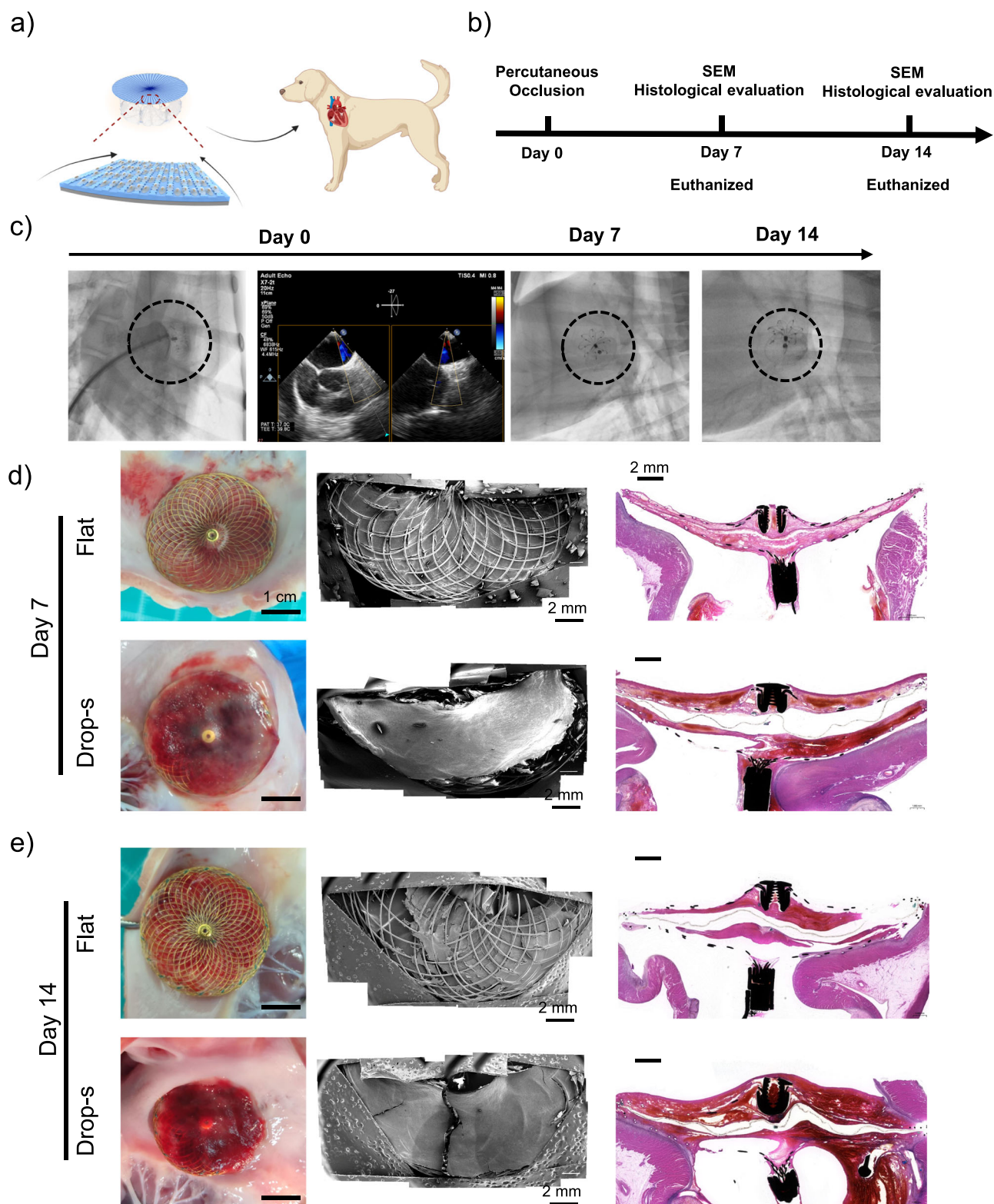


**Fig. 5 | Implantation of the LAA occluder in the canine model. a** Illustration of transcatheter interventional closure of LAA with the occluder. Created in BioRender. Ji, J. (2025) <https://BioRender.com/n35z026>. **b** Illustration of the study design. **c** Transthoracic echocardiography (TTE) examination during the LAA occlusion. The black dashed circle represents the location of LAA occluder.

Angiography image after 7 days and 14 days implantation. Photographs and representative SEM images of the neo-endocardium coverage on the flat occluder and drop-s occluder at 7 days (**d**) and 14 days (**e**). Scale bars, 1 cm in the photographs, 2 mm in the SEM images, and 2 mm in the H&E photograph.

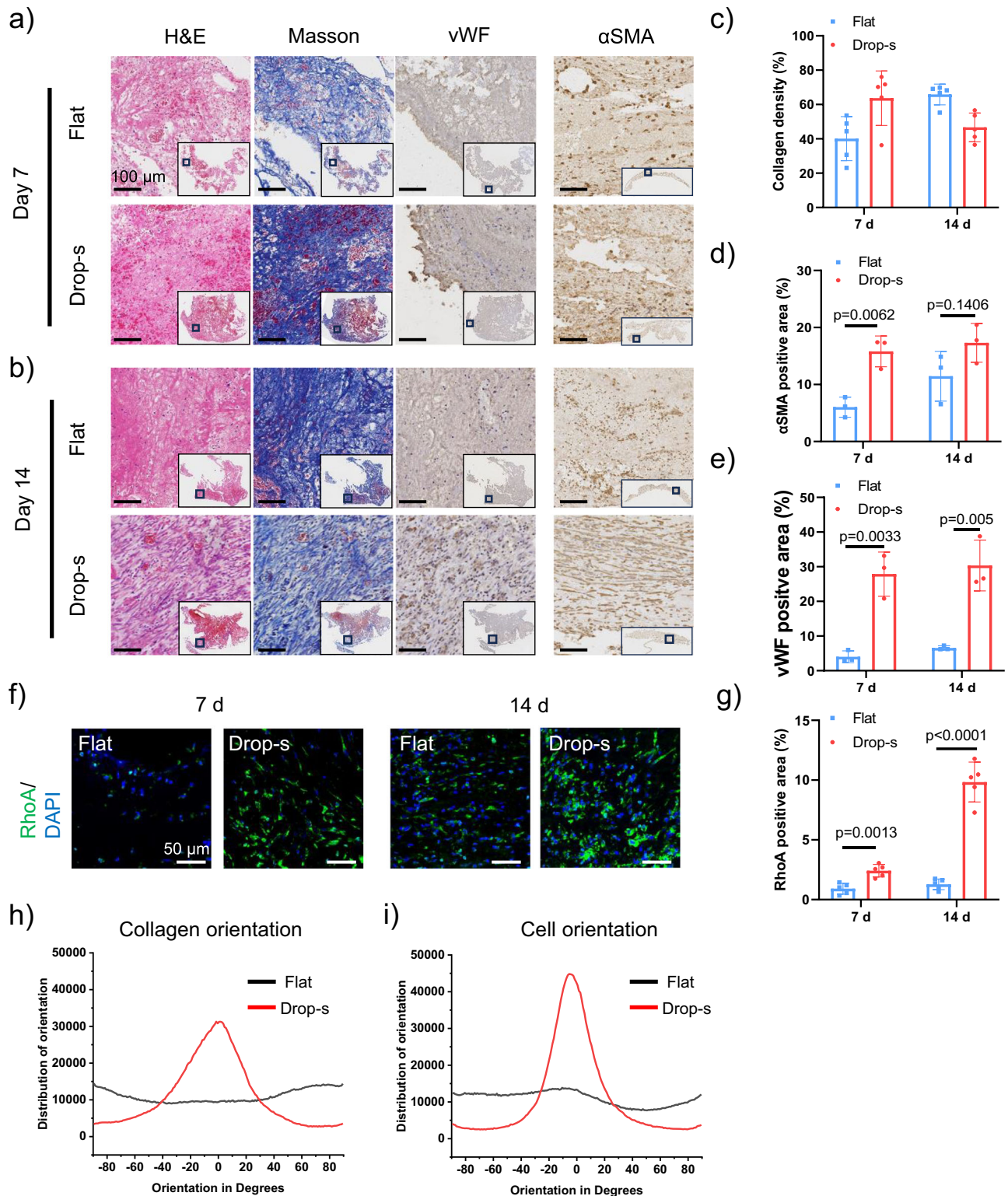


**Fig. 6 | Histologic examinations of the LAA occluders implanted in the canine LAA.** H&E staining, Masson staining, vWF staining and αSMA staining of neo-tissue on flat and Drop-s surface at 7 days (a) and 14 days (b). Quantitative results of collagen density (c), αSMA-positive area (d), and vWF-positive area (e) at 7 days and 14 days (Five measurements of collagen density and three measurements of positive area were taken for 5 different fields of view from 3 different regions of tissue). f Images of RhoA staining (green) and DAPI (blue) of the neo-

tissue at 7 days and 14 days. g Quantitative results of RhoA-positive area (Five measurements of RhoA-positive area were taken for 5 different fields of view from 3 different regions of tissue). Quantitative analysis of collagen orientation (h) and cell orientation (i) results based on tissue section images. The data were expressed as the mean ± SD. Significance determined by unpaired two-tailed *t*-test and *p* > 0.05 was considered as not significant.



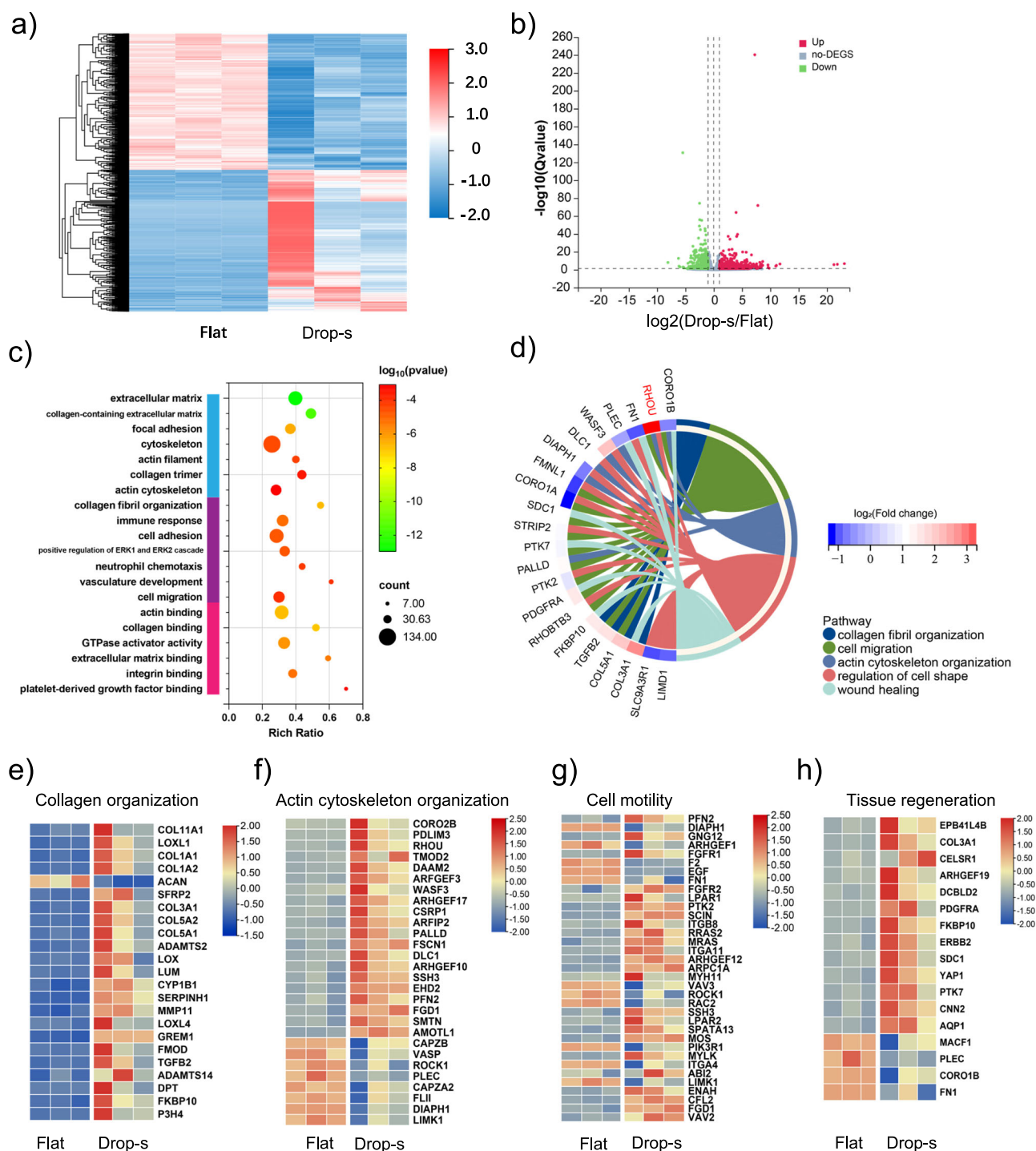


**Fig. 7 | The RNA-seq transcriptome analysis of the tissue collected from the surface of the occluder disk. a** Heatmap of differential genes. **b** Volcano map of significantly upregulated (red) and downregulated (blue) genes in different groups. **c** Bubble chart of differential gene enrichment (GO term). Hypergeometric test and

Benjamini–Hochberg *P* value correction algorithm were used to determine enriched GO terms. **d** Gene enrichment circle chart. Expression changes of collagen organization genes (**e**), actin cytoskeleton organization genes (**f**), cell motility genes (**g**), and tissue regeneration genes (**h**).

occluder in this study because the occluding disk of the disk-type occluder is relatively flat and has a larger area. In our study, the microgrooves were transferred to the surface of the occluding membrane by covering a PET fiber membrane on the occluding disk with PDMS and then curing it on a template. If a ball-type occluder is used, the microgrooves can also be fixed on the PET fiber membrane on the top of the device in the same way. However, the occluding surface of the ball-type occluder is not flat, which may affect the microgrooves

and lead to differences in the endothelialization speed. Another point worthy of attention is the extent of the gap between the LAA occluder and the LAA wall. Usually, the occluding disk needs to be closely attached to the left atrial appendage (LAA) wall to avoid residual shunt. But in reality, residual shunt may still occur<sup>47</sup>. In such cases, the endothelial cells on the LAA wall may not be able to come into contact with the microgrooves, resulting in partial incomplete endothelialization<sup>47</sup>.



In summary, we report here a drop-shaped microgroove on the LAA occluder, a practical interventional medical device, and demonstrate the potential of microgrooves to accelerate the coverage of new tissue on the surface and promote endothelialization. Cell experiments have shown that this microgroove effectively restricts the cytoskeleton and can guide the unidirectional migration of cells. Cells tend to migrate from the tail (wider area) to the head (narrower area) of the droplet within the groove, crossing the neck and entering the tail of the next unit. The migration of cells from the tail over the neck into the head is restricted. Our data indicate that this process is mainly related to the polarization of the cytoskeleton guided by the asymmetric structure at the neck. When crossing the neck, keratin polarizes at the cell's rear end (the wider area), propelling the cell forward, and this continuous process enables the cell to migrate in a single direction within the groove. We further verified the impact of this migration pattern on collective cell migration. Through code simulation and cell experiments, we found that the unidirectional migration of cells makes the efficiency of cell coverage in the central area higher. Our work holds promise for providing a practical solution to promote endothelialization on the surface of medical devices. This approach could potentially enhance the biocompatibility and functionality of such devices, leading to better clinical outcomes and patient safety.

## Methods

### Ethical statement

The rat experiment was approved by the Dr. Can Biotechnology (Zhejiang) Co., Ltd of Animal Ethics Committee and conducted in compliance with the ethical standards required by law and the guidelines for the use of experimental animals in China. All the canine experiments were approved by the Institutional Animal Care and Use Committee, Shenzhen Advanced Medical Services Co., Ltd (AMS F 2410003D), China.

### Fabrication of the substrates with microtopography

The microgrooves are radially arranged on a circular PET membrane, starting from the center, with a microgroove every 0.5 degrees, and the narrowest spacing between the grooves initially being 5 micrometers. The original microstructured silicon wafer was fabricated using classical photolithography procedures by UV illumination (MJB4 Mask Aligner, 23 mW/cm<sup>2</sup> power lamp, SUSS MicroTec, Germany) of a layer of SU8-2005 (MicroChem, USA) through a hard chromium mask. After exposure to vapor of trichloro (1H,1H,2H,2H-perfluorooctyl) silane (Sigma) for 20 min, the silicon wafer was used to create polydimethylsiloxane (PDMS Sylgard 184, Sigma Aldrich, ratio 1:10) replicates.

For the combination of the flat surface or microgrooves with the occluder, we removed the PET fiber membrane from the occluder disk, dipped it in PDMS, and then cured it on the template with flat surface (Flat) or drop-shaped microgrooves surface (Drop-s) (80 °C, 1 h). In this way, the PDMS with microstructures was coated on the fiber membrane. Finally, we sewed the fiber membrane with flat surface or drop-shaped microgrooves surface PDMS coating into the occluder disk to assemble a complete occluder.

### Characterization of the microtopography

The morphology of the PDMS was acquired by scanning electron microscope (SEM, Hitachi S4800) and fluorescence microscope (Nikon DS-Ri2). The depth of the microgrooves was acquired by Probe Profiler (Tencor D-100).

### Cell culture

Human umbilical vein endothelial cells (HUVECs) and human Aortic smooth muscle cells (SMCs) were purchased from ScienCell Research Laboratories (USA). Human microvascular endothelial cells (HCMEC/D3) were purchased from Procell (CL-0843, China). The cells were cultured

in an incubator (Thermo, USA) with a humidified atmosphere containing 5% CO<sub>2</sub> at 37 °C, and the medium for HUVECs and HCMEC/D3 was composed of endothelial cell growth medium (ScienCell) supplemented with 5% fetal bovine serum (FBS, ScienCell), penicillin (100 units/mL), and streptomycin (0.1 mg/mL).

### Characterization of cell behavior on the microgrooves

The morphology of HUVECs and SMCs was characterized after 1 day culture on the PDMS. All samples were gently washed with PBS, fixed with 4% paraformaldehyde, and treated with 0.1% Triton X-100. Cell staining was performed for nuclei (1:100, DAPI, Sigma), F-actin (FITC-phalloidine, Sigma) and Vinculin (anti-Vinculin, Sigma). The cell circularity, spreading area, and orientation were measured by ImageJ.

For the proliferation test, HUVECs were first stained by CMTPIX Dye or CellTracker™ Green CMFDA. Then, the HUVECs were seeded on the surface of samples and cultured for 4 h, 24 h, and 72 h. The cells were counted using ImageJ software.

### Characterization of cell migration on the surface

For the cell migration test, we covered the central flat or microgroove area with a 2 cm diameter circular PDMS patch and seeded cells around it for 24 h of culture. After removing the patch, we observed the progress of cell coverage in the central area with a microscope every 24 h. The uncovered area in the center was quantified using ImageJ.

Live recordings of HUVECs migration were performed after 24 h of culture with an automated inverted microscope (Olympus IX83) equipped with temperature and CO<sub>2</sub> regulation and controlled by the Cellsens software (Olympus). Images were acquired with a 20X objective for 2 h at 10 min intervals. The trajectories, directionality ratio, and speed of cell migration were evaluated using previously reported methods<sup>48</sup>.

### Live quantification of RhoA activity during cell migration

The RhoA activity was detected using fluorescence resonance energy transfer (FRET) biosensor<sup>49</sup>. HUVECs on different samples were transiently transfected lentiviral vectors expressing RhoA2G (pTriExRhoA2G) using the TurboFect reagent (ThermoFisher Scientific) according to the manufacturer's recommendations. The lentiviral vectors pTriExRhoA2G were a gift from Olivier Pertz (Addgene plasmid # 40176)<sup>49</sup>. The living cell fluorescence was observed with a confocal laser scanning microscope (Olympus FV3000-OSR).

### Simulation of the cell migration

We used a random walk model in MATLAB to simulate the coverage speed of cells on flat and microgrooves. We defined a plane with dimensions of 5 × 5 cm and set a circular void with a diameter of 2 cm in the center, where dots were used to represent cells. We set two main parameters: (1) The step length of cell migration (representing the speed of cell migration); (2) The probability of cells migrating towards the center (representing the directionality ratio of cell migration). These two parameters were derived from the directionality ratio of cell migration and the migration speed obtained through experiments in Fig. 2b, c. We continuously looped to update the position of each cell until some cells reached the exact center of the plane and then ended the loop. We output the cell position map every 10 steps and used particle image velocimetry (PIV) lab in MATLAB to analyze the cell migration process to generate the streamline diagram and direction vector of the cell flow.

### Wound healing model

Male 8-week-old Sprague Dawley rats (Dr. Can Biotechnology, China) were used for animal experiments. Rat experiment was approved by the Dr. Can Biotechnology (Zhejiang) Co., Ltd of Animal Ethics Committee and conducted in compliance with the ethical standards required by law and the guidelines for the use of experimental animals

in China. The findings apply to multiple sexes. This study did not intend to focus on a single sex. The hair on the dorsal surface of the rats was shaved using a depilatory cream. Isoflurane was used to induce anesthesia in the rats, and then a continuous flow of isoflurane was maintained to keep them anesthetized. Under sterile conditions, full-thickness circular excision wounds with a diameter of 12 mm were created on the dorsal skin using a biopsy punch. Samples with different surface topography (Flat, Parallel, and Drop-s) were stacked and implanted in the wound area. There were three wounds on the dorsal surface of each rat. In total, there were 3 rats. Each rat had the same wound location on its back, but the order of the samples was different on different rats to avoid errors caused by the sample location. The wound size was measured using ImageJ software.

### Platelet adhesion and activation assay

Whole blood was obtained from New Zealand white rabbits. Platelet-rich plasma (PRP) was obtained by centrifuging fresh rabbit blood at  $220\times g$  for 10 min. The different PDMS samples with different surface topographies were incubated with PRP for 2 h at 37 °C, then rinsed with PBS solution. Platelets were fixed with 2.5% glutaraldehyde/PBS solution for 30 min, dehydrated with graded ethanol/PBS solution (20%, 40%, 50%, 60%, 70%, 80%, 90%, 100%) for 15 min each, and then photographed by SEM (Hitachi, S4800).

### Immunostaining, imaging, and quantification

The samples were excised, fixed in 4% paraformaldehyde, and embedded in paraffin, and the samples were further processed for histology and immunohistochemistry. Cells on flat and micropillar surfaces were fixed and permeabilized with 0.1% Triton X-100 followed by blocking with 1% bovine serum albumin solution. Then, the primary antibodies were diluted in blocking solution and incubated with cells at 4 °C overnight. Primary antibodies: anti-vinculin (catalog no. MA5-14029, Invitrogen, IF: 1:100), anti- $\alpha$ SMA (catalog no. A5228, sigma, IHC: 1:200), anti-CD31 (catalog no. 14-0311-82, Invitrogen, IF: 1:100), anti-CD206 (catalog no. ab300622, Abcam, IF: 1:200), anti-CD68 (catalog no. ab283654, Abcam, IF: 1:200), anti-RhoA (catalog no. AF6352, Affinity Biosciences, IF: 1:100), and anti-vWF (catalog no. ab6994, Abcam, IHC: 1:200). For F-actin the FITC- phalloidin (catalog no. A12379, Alexa Fluor™ 488, Invitrogen) was used. After washing with a PBS buffer, secondary antibodies were diluted in PBS and incubated with cells at room temperature for 1 h. The nuclei were stained with 4',6-diamidino-2-phenylindole (DAPI; Sigma, 1:50). The staining was observed with a confocal laser scanning microscope (Olympus FV3000-OSR). Histology images were analyzed using ImageJ.

For the immunostaining of tissue, the tissues on the sample surfaces in rats or dogs were washed in 0.1 M sodium phosphate buffer, then incubated overnight at 2 °C to 8 °C in a primary antibody directed against collagen I (in the rat model, 14695-1-AP, Proteintech, IF: 1:100) and  $\alpha$ SMA (in the canine model, 14395-1-AP, Proteintech, IF: 1:100). The antibody reaction was then visualized with secondary antibodies (Invitrogen, Carlsbad, CA dilution 1:150). The staining was observed with a confocal laser scanning microscope (Olympus FV3000-OSR). The collagen and cell orientation were counted using the OrientationJ plug-in of ImageJ (NIH, Bethesda, USA). All antibodies were purchased from the supplier as noted above, and used according to the manufacturer's recommendations without additional validation.

### Canine model implantation and histopathology evaluation

All the canine experiments were approved by the Institutional Animal Care and Use Committee, Shenzhen Advanced Medical Services Co., Ltd (AMS F 2410003D), China. Twelve dogs (Labrador, 6 males and 6 females, 1 year old, 20–30 Kg) with a total of 12 Lifetech LAMBRE™ LAA Closure System were used in this study following the guidelines of the Chinese Animal Care and Use Committee standards. The devices were deployed under Intra-cardiac echocardiography (ICE). The device

position and stability were confirmed by transthoracic echocardiography (TTE) before releasing each device. After deployment, TTE was performed to evaluate device position and leakage around the device. The findings apply to multiple sexes. This study did not intend to focus on a single sex.

### Histological evaluation

After 7 days or 14 days, animals were euthanized, and a necropsy was performed. LAAs with implants were collected from all animals at necropsy. The samples were fixed in 10% formalin. The fixed samples were observed by SEM. Then the LAA device and the surrounding LA wall were dehydrated in a graded series of ethanol, followed by infiltration, and were embedded in methyl-methacrylate plastic for hematoxylin and eosin (H&E) staining. Endothelialization and neo-tissue formation were evaluated by immunohistochemistry staining of typical markers, including vWF,  $\alpha$ SMA and RhoA.

### Quantitative PCR and RNA-seq analysis

Total RNA was extracted using TRIzol reagent (Invitrogen, USA) from the skin around the wound of rats in quantitative PCR and tissue on the LAA occluder in RNA-seq analysis. The RNA libraries were sequenced by MajorBio Technology CO., Ltd (Shanghai, China). TPM (transcript per million) was used to measure the gene expression in RNA-seq. The differentially expressed genes (DEGs) were selected with fold change  $>2$  or fold change  $<0.5$  and  $p$ -value  $<0.05$  by R package. The protein-protein associations were analyzed by STRING. Quantitative real-time PCR (qRT-PCR) was performed with Power SYBR Green Master Mix (Applied Biosystems) following the manufacturer's guidelines. qRT-PCR was carried out on a Real-Time PCR Detection System (CFX384, Bio-Rad, USA), using the recommended settings for quantitative and relative expression analysis. Primer sequences used for qRT-PCR are detailed in Supplementary Table 1.

### Statistics and reproducibility

At least three times each experiment was repeated independently with similar results for Figs. 1c, d, 5d, e. All the experimental data were obtained from at least three independent experiments and expressed as the mean  $\pm$  standard deviation (SD). Statistical significance ( $p$ ) was assessed with unpaired two-tailed Student's  $t$ -test or two-side one-way analysis of variance (ANOVA) with Bonferroni multiple comparison correction using SPSS Statistics 26.0, where  $*p < 0.05$  was considered as significant and  $p > 0.05$  was considered not significant (n.s.). The schemes and illustrations were produced by Adobe Illustrator 2024 and Biorender (biorender.com).

### Reporting summary

Further information on research design is available in the Nature Portfolio Reporting Summary linked to this article.

### Data availability

The data generated in this study are provided in the Supplementary Information/Source Data file. The raw sequence data in this study have been deposited to the Genome Sequence Archive (GSA) in BIG Data Center, Beijing Institute of Genomics (BIG) with accession numbers of CRA020552. Source data are provided with this paper.

### Code availability

This study simulates cell migration using MATLAB software. The code for simulation in this study has been deposited in Zenodo at <https://doi.org/10.5281/zenodo.14699724>.

### References

- Hart, R. G., Pearce, L. A. & Aguilar, M. I. Meta-analysis: antithrombotic therapy to prevent stroke in patients who have non-valvular atrial fibrillation. *Ann. Intern. Med.* **146**, 857–867 (2007).

2. Saposnik, G., Gladstone, D., Raptis, R., Zhou, L. & Hart, R. G. Atrial fibrillation in ischemic stroke. *Stroke* **44**, 99–104 (2013).
3. Katsanos, A. H., Kamel, H., Healey, J. S. & Hart, R. G. Stroke prevention in atrial fibrillation. *Circulation* **142**, 2371–2388 (2020).
4. Caliskan, E. et al. Interventional and surgical occlusion of the left atrial appendage. *Nat. Rev. Cardiol.* **14**, 727–743 (2017).
5. Liuzzo, G. & Patrono, C. Occluding to prevent occlusion. *Eur. Heart J.* **42**, 3224–3225 (2021).
6. Turagam, M. K. et al. Cardiovascular therapies targeting left atrial appendage. *J. Am. Coll. Cardiol.* **72**, 448–463 (2018).
7. Lin, C., Liu, L. W., Liu, Y. J. & Leng, J. S. Recent developments in next-generation occlusion devices. *Acta Biomater.* **128**, 100–119 (2021).
8. Wang, Y., Li, G., Yang, L., Luo, R. & Guo, G. Development of innovative biomaterials and devices for the treatment of cardiovascular diseases. *Adv. Mater.* **34**, 2201971 (2022).
9. Ellis, C. R., Alkhouli, M., Anderson, J. A. & Swarup, V. Comparative endothelialization of Amulet LAA Occluder and Watchman 2.5 LAA device: observations from explanted hearts. *JACC Clin. Electrophysiol.* **8**, 828–829 (2022).
10. Sharma, S. P., Singh, D., Nakamura, D., Gopinathannair, R. & Lakireddy, D. Incomplete endothelialization of Watchman™ device: predictors and implications from two cases. *J. Atr. Fibrillation* **11**, 2162 (2019).
11. Dukkhipati, S. R. et al. Device-related thrombus after left atrial appendage closure: incidence, predictors, and outcomes. *Circulation* **138**, 874–885 (2018).
12. Fauchier, L. et al. Device-related thrombosis after percutaneous left atrial appendage occlusion for atrial fibrillation. *J. Am. Coll. Cardiol.* **71**, 1528–1536 (2018).
13. Otsuka, F. et al. The importance of the endothelium in atherothrombosis and coronary stenting. *Nat. Rev. Cardiol.* **9**, 439–453 (2012).
14. Wang, X. W. et al. UV-triggered hydrogel coating of the double network polyelectrolytes for enhanced endothelialization. *Adv. Sci.* **11**, 2401301 (2024).
15. Saliba, W. I. et al. Enhanced thromboresistance and endothelialization of a novel fluoropolymer-coated left atrial appendage closure device. *JACC Clin. Electrophysiol.* **9**, 1555–1567 (2023).
16. Trimm, E. & Red-Horse, K. Vascular endothelial cell development and diversity. *Nat. Rev. Cardiol.* **20**, 197–210 (2023).
17. Curtis, A. S. G. & Wilkinson, C. D. W. Reactions of cells to topography. *J. Biomater. Sci. Polym. Ed.* **9**, 1313–1329 (1998).
18. Ko, Y.-G., Co, C. C. & Ho, C.-C. Directing cell migration in continuous microchannels by topographical amplification of natural directional persistence. *Biomaterials* **34**, 353–360 (2013).
19. Yang, Y., Xu, T., Bei, H. P., Zhao, Y. & Zhao, X. Sculpting bio-inspired surface textures: an adhesive Janus periosteum. *Adv. Funct. Mater.* **31**, 2104636 (2021).
20. Wang, X. L. et al. Chromatin reprogramming and bone regeneration in vitro and in vivo via the microtopography-induced constriction of cell nuclei. *Nat. Biomed. Eng.* **7**, 1514 (2023).
21. Vedula, S.R.K. et al. Emerging modes of collective cell migration induced by geometrical constraints. *Proc. Natl Acad. Sci. USA* **109**, 12974–12979 (2012).
22. Leclech, C. et al. Topography-induced large-scale antiparallel collective migration in vascular endothelium. *Nat. Commun.* **13**, 2797 (2022).
23. Yi, B. C., Zhou, B. Y., Dai, W. F., Lu, X. W. & Liu, W. Soft nanofiber modified micropatterned substrates enhance native-like endothelium maturation via CXCR4/calcium-mediated actin cytoskeleton assembly. *Nano Res.* **16**, 792–809 (2023).
24. Kang, I.-G. et al. Bioactive and mechanically stable hydroxyapatite patterning for rapid endothelialization of artificial vascular graft. *Mater. Sci. Eng. C* **106**, 110287 (2020).
25. Yi, B. et al. Step-wise CAG@PLys@PDA-Cu<sup>2+</sup> modification on micropatterned nanofibers for programmed endothelial healing. *Bioact. Mater.* **25**, 657–676 (2023).
26. Yao, Y. et al. Fucoidan and topography modification improved in situ endothelialization on acellular synthetic vascular grafts. *Bioact. Mater.* **22**, 535–550 (2023).
27. Kushiro, K., Chang, S. & Asthagiri, A. R. Reprogramming directional cell motility by tuning micropattern features and cellular signals. *Adv. Mater.* **22**, 4516–4519 (2010).
28. Mahmud, G. et al. Directing cell motions on micropatterned ratchets. *Nat. Phys.* **5**, 606–612 (2009).
29. Le Maout, E., Lo Vecchio, S., Kumar Korla, P., Jinn-Chyuan Sheu, J. & Riveline, D. Ratchetaxis in channels: entry point and local asymmetry set cell directions in confinement. *Biophys. J.* **119**, 1301–1308 (2020).
30. Lamalice, L., Le Boeuf, F. & Huot, J. Endothelial cell migration during angiogenesis. *Circ. Res.* **100**, 782–794 (2007).
31. Du, Y. et al. Dynamics of endothelial cells migration in nature-mimicking blood vessels. *Talanta* **277**, 126415 (2024).
32. Jerka, D. et al. Unraveling endothelial cell migration: insights into fundamental forces, inflammation, biomaterial applications, and tissue regeneration strategies. *ACS Appl. Bio Mater.* **7**, 2054–2069 (2024).
33. Wang, X. L. et al. The combined contribution of vascular endothelial cell migration and adhesion to stent re-endothelialization. *Front. Cell Dev. Biol.* **9**, 641382 (2021).
34. Yang, L. et al. Research progress on the regulatory mechanism of integrin-mediated mechanical stress in cells involved in bone metabolism. *J. Cell. Mol. Med.* **28**, e18183 (2024).
35. Li, X., Combs, J. D., Salaita, K. & Shu, X. Polarized focal adhesion kinase activity within a focal adhesion during cell migration. *Nat. Chem. Biol.* **19**, 1458–1468 (2023).
36. Loschke, F., Seltmann, K., Bouameur, J.-E. & Magin, T. M. Regulation of keratin network organization. *Curr. Opin. Cell Biol.* **32**, 56–64 (2015).
37. Shimokawa, H., Sunamura, S. & Satoh, K. RhoA/Rho-kinase in the cardiovascular system. *Circ. Res.* **118**, 352–366 (2016).
38. Petrie, R. J., Doyle, A. D. & Yamada, K. M. Random versus directionally persistent cell migration. *Nat. Rev. Mol. Cell Biol.* **10**, 538–549 (2009).
39. Jana, S. Endothelialization of cardiovascular devices. *Acta Biomater.* **99**, 53–71 (2019).
40. Weijs, B. et al. Blood flow-induced Notch activation and endothelial migration enable vascular remodeling in zebrafish embryos. *Nat. Commun.* **9**, 5314 (2018).
41. Markl, M. et al. Left atrial and left atrial appendage 4D blood flow dynamics in atrial fibrillation. *Circ. Cardiovasc. Imaging* **9**, e004984 (2016).
42. Tewari, P., Mammen, A., Pandey, S., Ahmad, S. S. & Hajela, K. Left atrial appendage (LAA) flow profile of its different waves and its correlation with direct left atrial pressure measurement: can LAA flow profile be a surrogate to estimate left atrial pressure. *Ann. Card. Anaesth.* **25**, 48–53 (2022).
43. Aitken, C., Mehta, V., Schwartz, M. A. & Tzima, E. Mechanisms of endothelial flow sensing. *Nat. Cardiovasc. Res.* **2**, 517–529 (2023).
44. McDonald, T. P. The regulation of megakaryocyte and platelet production. *Int. J. Cell Cloning* **7**, 139–155 (1989).
45. Ding, Y. et al. Effects of microtopographic patterns on platelet adhesion and activation on titanium oxide surfaces. *J. Biomed. Mater. Res. A* **101A**, 622–632 (2013).
46. McWhorter, F. Y., Wang, T., Nguyen, P., Chung, T. & Liu, W. F. Modulation of macrophage phenotype by cell shape. *Proc. Natl Acad. Sci. USA* **110**, 17253–17258 (2013).
47. Chen, T. et al. Occlusion of bilobulated left atrial appendage using the dual-watchman technique: a long-term follow-up study. *Front. Cardiovasc. Med.* **9**, 854475 (2022).



48. Gorelik, R. & Gautreau, A. Quantitative and unbiased analysis of directional persistence in cell migration. *Nat. Protoc.* **9**, 1931–1943 (2014).
49. Fritz, R. D. et al. A versatile toolkit to produce sensitive FRET biosensors to visualize signaling in time and space. *Sci. Signal.* **6**, rs12 (2013).

## Acknowledgements

This work was supported by the Zhejiang Provincial Natural Science Foundation of China (No. LD22E030008, L.Y.), the National Natural Science Foundation of China (No. U20A20262, K.R.), and the Medical Health Science and Technology Project of Zhejiang Provincial Health Commission (No. 2022483477, L.Y.). This work was also supported by Zhejiang University K. P. Chao's High Technology Development Foundation (K.R.).

## Author contributions

X.W. and C.Y. performed major experiments, characterizations and data analysis. X.W. wrote the initial manuscript. Q.T. participated in drawing. H.Y. participated in experiments. G.F. and J.W. contributed to the data discussion. J.J., K.R., and L.Y. conceived and supervised the project, revised and reviewed the manuscript.

## Competing interests

J.J., K.R., X.W., J.W., G.F., and L.Y. are inventors of a patent related to this work filed by Zhejiang University (2023106046243), the remaining authors declare no competing interests.

## Additional information

**Supplementary information** The online version contains supplementary material available at <https://doi.org/10.1038/s41467-025-57146-5>.

**Correspondence** and requests for materials should be addressed to Ke-feng Ren, Lu Yu or Jian Ji.

**Peer review information** *Nature Communications* thanks Deirdre Anderson and Jai-Wun Park for their contribution to the peer review of this work. A peer review file is available.

**Reprints and permissions information** is available at <http://www.nature.com/reprints>

**Publisher's Note** Springer Nature remains neutral with regard to jurisdictional claims in published maps and institutional affiliations.

**Open Access** This article is licensed under a Creative Commons Attribution-NonCommercial-NoDerivatives 4.0 International License, which permits any non-commercial use, sharing, distribution and reproduction in any medium or format, as long as you give appropriate credit to the original author(s) and the source, provide a link to the Creative Commons licence, and indicate if you modified the licensed material. You do not have permission under this licence to share adapted material derived from this article or parts of it. The images or other third party material in this article are included in the article's Creative Commons licence, unless indicated otherwise in a credit line to the material. If material is not included in the article's Creative Commons licence and your intended use is not permitted by statutory regulation or exceeds the permitted use, you will need to obtain permission directly from the copyright holder. To view a copy of this licence, visit <http://creativecommons.org/licenses/by-nc-nd/4.0/>.

© The Author(s) 2025